SCIENTIFIC REPORTS

OPEN

SUBJECT AREAS:
CATALYTIC MECHANISMS
FUEL CELLS

Received
21 February 2014

Accepted
19 May 2014

Published
6 June 2014

Correspondence and requests for materials should be addressed to Y.F.Z. (yfzhu@jlu.edu.cn) or Q.J. (jiangq@jlu.edu.cn)

$Al_{13}@Pt_{42}$ Core-Shell Cluster for Oxygen Reduction Reaction

B. B. Xiao, Y. F. Zhu, X. Y. Lang, Z. Wen & Q. Jiang

Key Laboratory of Automobile Materials, Ministry of Education, and School of Materials Science and Engineering, Jilin University, Changchun 130022, China.

To increase Pt utilization for oxygen reduction reaction (ORR) in fuel cells, reducing particle sizes of Pt is a valid way. However, poisoning or surface oxidation limits the smallest size of Pt particles at 2.6 nm with a low utility of 20%. Here, using density functional theory calculations, we develop a core-shell $Al_{13}@Pt_{42}$ cluster as a catalyst for ORR. Benefit from alloying with Al in this cluster, the covalent Pt-Al bonding effectively activates the Pt atoms at the edge sites, enabling its high utility up to 70%. Valuably, the adsorption energy of O is located at the optimal range with 0.0–0.4 eV weaker than Pt(111), while OH-poisoning does not observed. Moreover, ORR comes from O_2 dissociation mechanism where the rate-limiting step is located at OH formation from O and H with a barrier of 0.59 eV, comparable with 0.50 eV of OH formation from O and H_2O on Pt(111).

Proton exchange membrane fuel cells (PEMFCs) are promising candidates for mobile and transport applications due to their high energy density, zero emissions, relatively low operating temperature, and minimal corrosion problems[1]. Pt nanoparticles supported on carbon are commonly used as catalysts of the cathode for the oxygen reduction reaction (ORR)[2]. It is observed that the ORR activity highly depends on the size of nanoparticles, where Pt nanoparticles with diameters (D) of 2–5 nm are regarded as the best[3,4]. This is because the percentage of atoms on the active Pt(111) facets over the total number of atoms n, denoting as $R_{(111)}$, reaches the maximum[2,5,6]. If the particle takes an (111)-enclosed icosahedral shape as shown in Figure 1, in order to maximize $R_{(111)}$, the corresponding D (D_c) is 2.6 nm with $n = 561$, which brings out $R_{(111)} = 20\%$. Further reducing D could increase the surface/volume ratio, and the percentages of edge and vertex sites (R_e and R_v) on the particle surfaces unfortunately increase where R_e becomes predominant below D_c. Those Pt atoms at the low-coordinated sites are adverse for ORR due to the strong binding of O-containing intermediates[4,7–10]. Thus, activating edge and vertex sites is the main challenge to miniaturize D.

As adsorption energies of all intermediates of ORR are related to the O adsorption energy [E_{ads}(O)] on (111) surfaces of transition metals, the activity is proposed to be a function of E_{ads}(O)[2,11–13]. It has demonstrated that E_{ads}(O) of a catalyst with the best activity for ORR should be 0.0–0.4 eV weaker than that of Pt(111)[2,9,13]. Furthermore, a volcano activity curve based on the adsorption energy of OH [E_{ads}(OH)] is present where E_{ads}(OH) is 0.0–0.2 eV weaker than that of Pt(111), due to the scaling relationship between E_{ads}(O) and E_{ads}(OH)[2,6,12,14]. Note that the coordination numbers of the vertex atoms and the edge atoms of nanoparticles differ from that of (111) surface of nine. Thus, the scaling relationship between E_{ads}(O) and E_{ads}(OH) may be changed and E_{ads}(O) and E_{ads}(OH) must be both inquired separately.

On the other hand, numerous experimental and theoretical studies have been carried out to study the kinetics of ORR mechanisms[2,15–18]. To our knowledge, there are mainly three mechanisms: O_2 dissociation, OOH dissociation and H_2O_2 dissociation. Qi *et al.* have demonstrated that in the gas phase, instead of the high barrier (E_a) of OH formation from O and H with a value of 0.91 eV, OH is originated from OOH and H with $E_a = 0.31$ eV[15,16]. However, this path is absent because H_2O_2 formation is forbidden in solution[17]. Recently, a new path is proposed: OH formation in solution comes from O and H_2O, and ORR on Pt(111) is essentially carried out by O_2 dissociation mechanism, namely O_2 dissociation (E_a = 0.00 eV), OH formation (E_a = 0.50 eV) and H_2O formation (E_a = 0.24 eV)[18]. It is doubted that whether ORR mechanism is changed due to the presence of the low-coordinated atoms at nano size. Thus, in order to fully understand the catalysis, the kinetics of ORR mechanisms needs to be further explored.

Alloying is a general technique to improve the ORR activity and stability of catalysts[13,14,19–21]. Present works have been mainly concentrated on Pt-based alloys consisting of Pt and the late TM elements in the 3*d* series, typically Pt_3Fe, Pt_3Co and Pt_3Ni. The alloys show better catalysis activity than Pt alone[22]. However, the severe degradation of catalysis and stability of these alloys during the voltage cycling in acids as a consequence of the

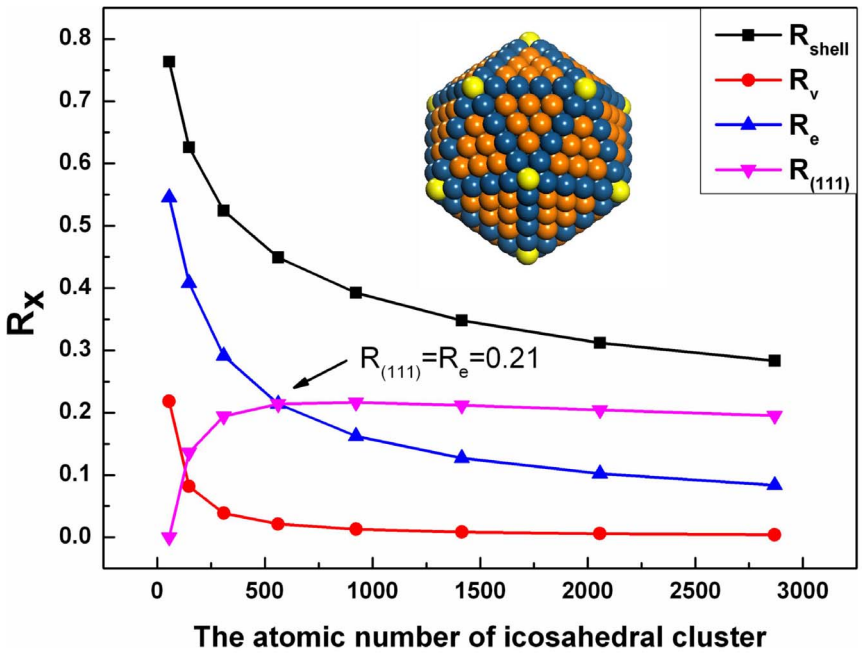

Figure 1 | Size-dependent percentage of atoms on (111), edge and vertex, expressed by $R_{(111)}$, R_e and R_v. R_{shell} denotes the percentage of atoms on the shell, and $R_{shell} = R_{(111)} + R_e + R_v$. Atoms in yellow, blue and orange denote Pt_v, Pt_e and $Pt_{(111)}$atoms. Inset is the structure of Pt_{561} where $R_e = R_{(111)}$.

continuous dissolution of TM atoms are present[22,23]. This can be understood by their negligible heat of formation[13,24]. Following the suggestion of Greeley et al., strong binding between Pt and other alloying elements is needed to improve the stability of any new alloy systems[13]. Since the formation energy of Pt_3Al is much more negative than Pt-based alloys with late TM elements[24], Pt_3Al should be a good substitute of the above Pt-based alloys. It must be admitted that Pt-based alloys with early TM elements show good activity and stability, such as Pt_3Sc and Pt_3Y[13,22]. However, these works are still located at the transition metals and the activity enhancement is resulted from the *d-d* interaction to modify the *d* band of Pt surface atoms[13,22]. Thus, from the electronic aspect, the *p-d* interaction of Al-Pt systems would provide an attempt to look beyond the Pt-TM systems and explore novel catalysts.

Recent DFT calculations show that a core-shell structure plays an important role in increasing the stability of Pt-based nanoalloys, such as $Co_{13}@Pt_{42}$ and $Rh_{13}@Pt_{42}$[25,26] where Pt shell benefits for the stability of the catalysts under the electrochemical environment[21,23,27–29]. Thus, we here develop a new core-shell $Al_{13}@Pt_{42}$ cluster as ORR catalyst, whose surface is assembled with the twelve vertex atoms Pt_v and the thirty edge atoms Pt_e. In addition, Al_{13} cluster with icosahedral symmetry have been shown to exhibit enhanced stability compared with other isomers[30,31]. What is more, the ligand stabilized Al nanoparticles with the size range of 1.5 and 4 nm have been synthesized[32,33]. It is noteworthy that although Al@Pt core-shell nanoparticles have not been synthesized to date, Al@Cu and Al@Co ones are fabricated via a displacement reaction[34,35]. Although these particles had large particle sizes about 5 μm, the utilized experimental technique could also be applied to fabricate Al@Pt core-shell nanostructures as long as the size of Al nanoparticles is small, which has been be synthesized without difficulties[32,33]. Note that although Al could be easily oxidized it has been easily avoided by an inert atmosphere[33]. At last, it is emphasized that our work offers only a theoretical prediction and we hope this new Al@Pt cluster will be picked up by experimentalists for empirical verification.

In light of our calculation by using Density Functional Theory (DFT), Al@Pt cluster possesses good stability due to the covalent bonding between Al_{13} core and Pt_{42} shell. Also, E_{ads}(O) is located at the optimal range while E_{ads}(OH) on Pt_e is 0.30 eV weaker than Pt(111). Furthermore, rate-limiting step (RDS) of the ORR reaction though O_2 dissociation mechanism is located at OH formation from O and H (E_a = 0.59 eV). This barrier is comparable with 0.50 eV of Pt(111)[18]. Thus, alloying with Al effectively activates Pt_e atoms and lets the utility of Pt reach 70% (30 edge Pt_e atoms from the total 42 Pt atoms).

Results

Figure 2(a) shows a core-shell $Al_{13}@Pt_{42}$ cluster (n = 55) with an icosahedral structure where 13 Al atoms form an icosahedral core and all Pt atoms are located on the shell. All Pt atoms are all low-coordinated, which consist of 6-coordination vertex atoms (Pt_v) and 8-coordination edge atoms (Pt_e). The $Al_{13}@Pt_{42}$ possesses a high symmetry and stability (the mean binding energy E_b = −4.8 eV/atom compared with −4.75 eV/atom of Pt_{55} according to our calculation). To understand physically the interaction between Al core and Pt shell of $Al_{13}@Pt_{42}$, partial density of states (PDOS) is shown in Figure 2(c). Compared with Pt_{55}, the *d* band of Pt_{42} shell on $Al_{13}@Pt_{42}$ is moved away from the Fermi energy E_F. That is, the *d* band center changes from −1.99 of Pt_{55} to −2.54 eV of $Al_{13}@Pt_{42}$. Furthermore, the *d* band of alloy cluster is clearly more discrete. The *d* band of Pt_{42} shell is concentrated in between 0 to −6.8 eV. For Al_{13} core, the *p* band has the same trend with the *d* band of Pt_{42} shell, which denotes the strong orbital hybridization. It is obvious that the *d* orbitals (at −1.7, −2.6, −3.4, −4.5, −5.5 and −6.3 eV) interact with the *p* orbitals (at −1.8, 2.6, −3.4, −4.9 and −6.3 eV) and weak *p-d* hybridization is present at −8.1 eV below E_F. On the other hand, the main of *s* band is located below −6.8 eV. Compared with *p-d* hybridization, the *s-d* interaction is weak, appearing at −5.1, −6.4, −7.4 and −8.1 eV below E_F. Therefore, the enhancement in stability is dominated by hybridization between Pt-5*d* band and Al-3*p* band. To confirm this interaction, the electron density difference Δρ calculated is presented in Figure 2(d). Obviously, electrons are accumulated between Pt and Al atoms, which are compatible with the observation of the corresponding PDOS and demonstrates the partial formation of the covalent Pt-Al bonds.

In order to further confirm the stability of $Al_{13}@Pt_{42}$, we consider the stability of $Fe_{13}@Pt_{42}$, $Co_{13}@Pt_{42}$ and $Ni_{13}@Pt_{42}$ for a compar-

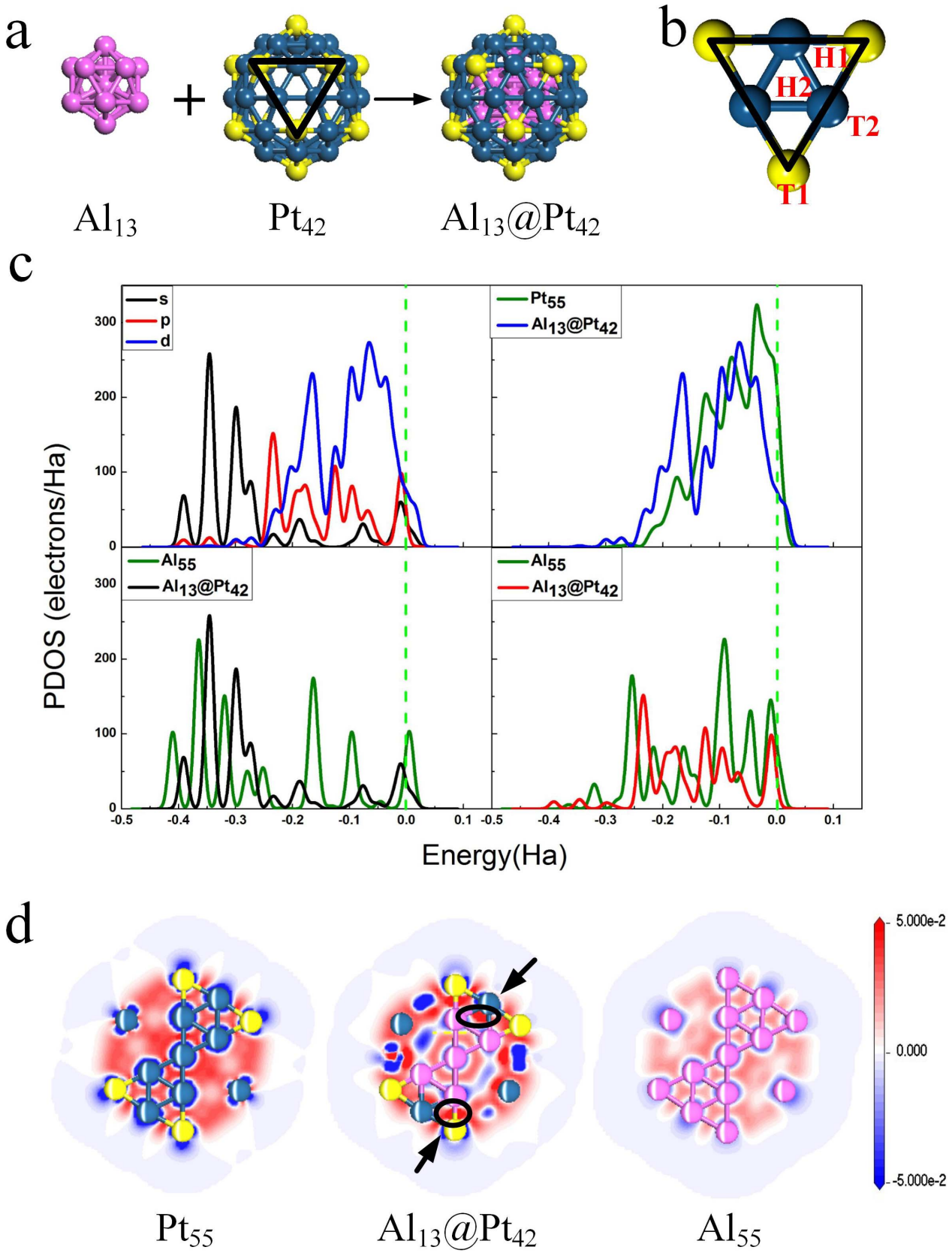

Figure 2 | (a) The structure of icosahedral $Al_{13}@Pt_{42}$ cluster. Atoms in yellow denotes vertex Pt_v, edge Pt_e atoms are in blue. Purple shows Al atoms. (b) The adsorption sites of high-symmetry on a triangular face. T1 and T2 top sites are located atop of Pt_v and Pt_e, respectively; H1 and H2 show hcp and fcc hollow sites respectively. The former is surrounded by Pt_v and Pt_e while the latter is surrounded by only Pt_e. (c) The partial density of states (PDOS). Top left is PDOS of $Al_{13}@Pt_{42}$. For clarity, the intensity of *d*-electrons is reduced to the one tenth. Top right is *d*-electron PDOS of Pt_{42} shell on Pt_{55} and $Al_{13}@Pt_{42}$. Bottom left and right are *s*- and *p*-electron PDOS of Al_{13} core in Al_{55} and $Al_{13}@Pt_{42}$. (d) The plot of electron density difference $\Delta\rho$.The loss and enrichment of electrons are indicated in blue and red. Here, Al_{55} denotes 55-atomic Al cluster with icosahedral shape.

Table 1 | The calculated core-shell interaction energies E_{cs} and the Pt_{42} shell dissolution potentials $U_{diss}(M_{13}@Pt_{42})$. The units are eV/atom and V, respectively

	Pt_{55}	$Al_{13}@Pt_{42}$	$Fe_{13}@Pt_{42}$	$Co_{13}@Pt_{42}$	$Ni_{13}@Pt_{42}$
E_{cs}	−0.52	−0.84	−0.75	−0.62	−0.53
$U_{diss}(M_{13}@Pt_{42})$	0.816	1.101	1.087	0.995	0.933

ison purpose as the three alloying elements have been well studied[36–38]. Table 1 lists the core-shell interaction energy E_{cs}, which could interpret enhanced phenomenon[13,26,39], and the dissolution potential $U_{diss}(M_{13}@Pt_{42})$ of the Pt_{42} shell in $M_{13}@Pt_{42}$ icosahedral clusters (M = Al, Fe, Co, Ni). It is found that due to the alloying, $U_{diss}(M_{13}@Pt_{42})$ of clusters are enhanced compared with that of Pt_{55}. That is, the stronger E_{cs} makes the higher dissolution resistance, which is similar to the relationship between the alloy formation energy and the ORR stability of the Pt_3M bulk[13,39]. The corresponding order is $Al_{13}@Pt_{42} > Fe_{13}@Pt_{42} > Co_{13}@Pt_{42} > Ni_{13}@Pt_{42} > Pt_{55}$. Thus, we expect that the stability of $Al_{13}@Pt_{42}$ acted as ORR catalysts is well.

$E_{ads}(O)$ and $E_{ads}(OH)$ on $Al_{13}@Pt_{42}$ are firstly examined. For comparison purpose, these values on Pt_{55} and Pt(111) are also calculated. According to previous studies, we focused on the adsorption of O on hollow sites and OH on atop sites as the adsorption sites shown in Figure 2(b)[13,40]. The corresponding $E_{ads}(O)$ and $E_{ads}(OH)$ values are listed in Table 2. The most favored $E_{ads}(O)$ and $E_{ads}(OH)$ values on Pt(111) are −4.51 on fcc site and −2.45 eV on atop site [the reported results are $E_{ads}(O) = -4.21$ eV and $E_{ads}(OH) = -2.31$ eV, respectively, being in accord with our data[41,42]]. For O adsorption on Pt_{55}, $E_{ads}(O)$ are −4.56 and −4.71 eV on H1 and H2 sites, respectively, which are stronger than that of Pt(111). Similarly, compared with Pt(111), OH adsorption are stronger with $E_{ads}(OH)$ of −3.13 eV on T1 site and −2.91 eV on T2 site. Therefore, Pt_{55} are both O and OH poisoned due to the enhanced adsorption ability of the low-coordinated Pt atoms[43]. On the other hand, for $Al_{13}@Pt_{42}$, $E_{ads}(O)$ are −4.15 and −4.25 eV on H1 and H2 sites, respectively, which are 0.36 and 0.26 eV weaker than that of Pt(111). Therein, the $E_{ads}(O)$ values are located at the optimal range for ORR[2,13]. For OH adsorption on T1 site, $E_{ads}(OH)$ is −2.81 eV and is 0.36 eV stronger compared with Pt(111). However, as OH on T2 site, $E_{ads}(OH)$ is 0.30 eV weaker than that of Pt(111) with a value of −2.15 eV. The scaling relationship between O and OH is broken on $Al_{13}@Pt_{42}$[11,12]. Although there is serious OH-poisoning at T1 site, OH-poisoning at T2 site is absent. Thus, OH adsorption on T2 site can easily be removed, and the recovery of T2 site for the next ORR cycle could take place. In light of viewpoint of OH-poisoning, it is likely that the only edge atoms (Pt_e) of $Al_{13}@Pt_{42}$ are effective for ORR.

The above results are supported by the relationship between electronic structures and atomic ones of $Al_{13}@Pt_{42}$. It is known that surface atoms with larger coordination number have a lower *d* band center and weaker adsorption ability[43]. For $Al_{13}@Pt_{42}$, the effective coordination number (N_{eff}) is proposed to show the effect of the Al alloying[44]. We carried out a simple linear regression analysis to correlate $E_{ads}(O)$ and $E_{ads}(OH)$ adsorbed on T1 and T2 sites with N_{eff} of Pt atom, $N_{eff} = N_{Pt} + XN_{Al}$, where subscripts show the corresponding elements, X is the effect coefficient of one Al atom corresponding one Pt atom for N_{eff}, which is obtained by fitting technique. By using this technique, X = 2.5 is obtained. That is, N_{eff} values of Pt_v and Pt_e on $Al_{13}@Pt_{42}$ are 7.5 and 11. The average N_{eff} value of Pt_{42} shell consisting of Pt_v and Pt_e is 10, being larger than 7.4 of Pt_{55} and 9 of Pt(111). The above atomic structural analysis corresponds to the fact that the *d* band center moves towards the lower-energy range from −1.99 eV of Pt_{55} to −2.54 eV of $Al_{13}@Pt_{42}$, which effectively illustrates that the presence of Al reduces the adsorption ability of the low-coordinated Pt atoms, as shown in Figure 2(c). On the other hand, the Mulliken charge analysis displayed in Figure 3(a) show that the electrons are transferred from the Al_{13} core to Pt_{42} shell, leading to the formation of negatively charged shell. Therein, the $Q(Pt_v)$ and $Q(Pt_e)$ are −0.185 and −0.380*e*, respectively (Q defines as the number of the transferred electrons). After O adsorption on H2 site, Q(O) and $Q(Pt_e)$ are −0.585 and −0.181*e*, respectively, which means the presence of electrostatic repulsion. However, a completely different situation is found on Pt(111). In Figure 3(b), Pt(111) is nearly electrically neutral with Q(Pt) = −0.006*e*. After O adsorption on fcc site, Q(O) and Q(Pt) are −0.548 and 0.149*e*, respectively. That is, the electrostatic attraction appears for O adsorption on Pt(111). It is plausible that the weaker $E_{ads}(O)$ of $Al_{13}@Pt_{42}$ is just due to this electrostatic repulsion between the electronegative O adatom and the Pt atoms[45,46]. In order to demonstrate the effect of the negative charges on $E_{ads}(O)$, we artificially add electrons Q_{add} on Pt(111) and then calculate the corresponding $E_{ads}(O)$[47]. In Figure 3(c), for O adsorption on Pt(111), the Q(Pt) sign is changed from positive to negative and Q(O) is more negative when Q_{add} is increased. Namely, the interaction between O and Pt(111) is changed from electrostatic attraction to electrostatic repulsion. As shown in Figure 3(d), $E_{ads}(O)$ is weakened as Q_{add} is increased. Furthermore, from the *d*-PDOS of the Pt(111) with different Q_{add} values shown in Figure 3(e), there is little change of the *d* band. Thus, the electrostatic repulsion indeed reduces the $E_{ads}(O)$. Since OH adsorption has a similar case of O adsorption, we do not show the corresponding results here. In summary, both electronic and atomic structures of $Al_{13}@Pt_{42}$ support its high poisoning resistance for ORR.

In order to characterize ORR catalyzed on the $Al_{13}@Pt_{42}$, the distinct reaction paths are considered to determine transition states and activation energies or energy barrier (E_a) using nudged elastic band theory (NEB) for all elemental reaction steps involved in ORR in Figure S1 and the corresponding data are listed in Table 3. Firstly, the O_2 dissociation mechanism, including O_2 dissociation, OH formation, and H_2O formation, is considered. The results are shown in Figure 4 and Table 3. For O_2 dissociation, the $E_a = 0.13$ eV. Figure S2 illustrates the spin-polarized partial density of states (PDOS)

Table 2 | The calculated adsorption energy values of $E_{ads}(O)$ and $E_{ads}(OH)$ on Pt_{55}, $Al_{13}@Pt_{42}$, and Pt(111) (The adsorption sites are described in caption of Figure 2b).The values in parentheses show differences between $E_{ads}(O)$ and $E_{ads}(OH)$ values on $Al_{13}@Pt_{42}$ and that on Pt(111)

	$E_{ads}(O)$		$E_{ads}(OH)$	
	H1	H2	T1	T2
Pt_{55}	−4.56(−0.05)	−4.71(−0.20)	−3.13(−0.68)	−2.91(−0.46)
$Al_{13}@Pt_{42}$	−4.15(0.36)	−4.25(0.26)	−2.81(−0.36)	−2.15(0.30)
Pt(111)	−4.51		−2.45	

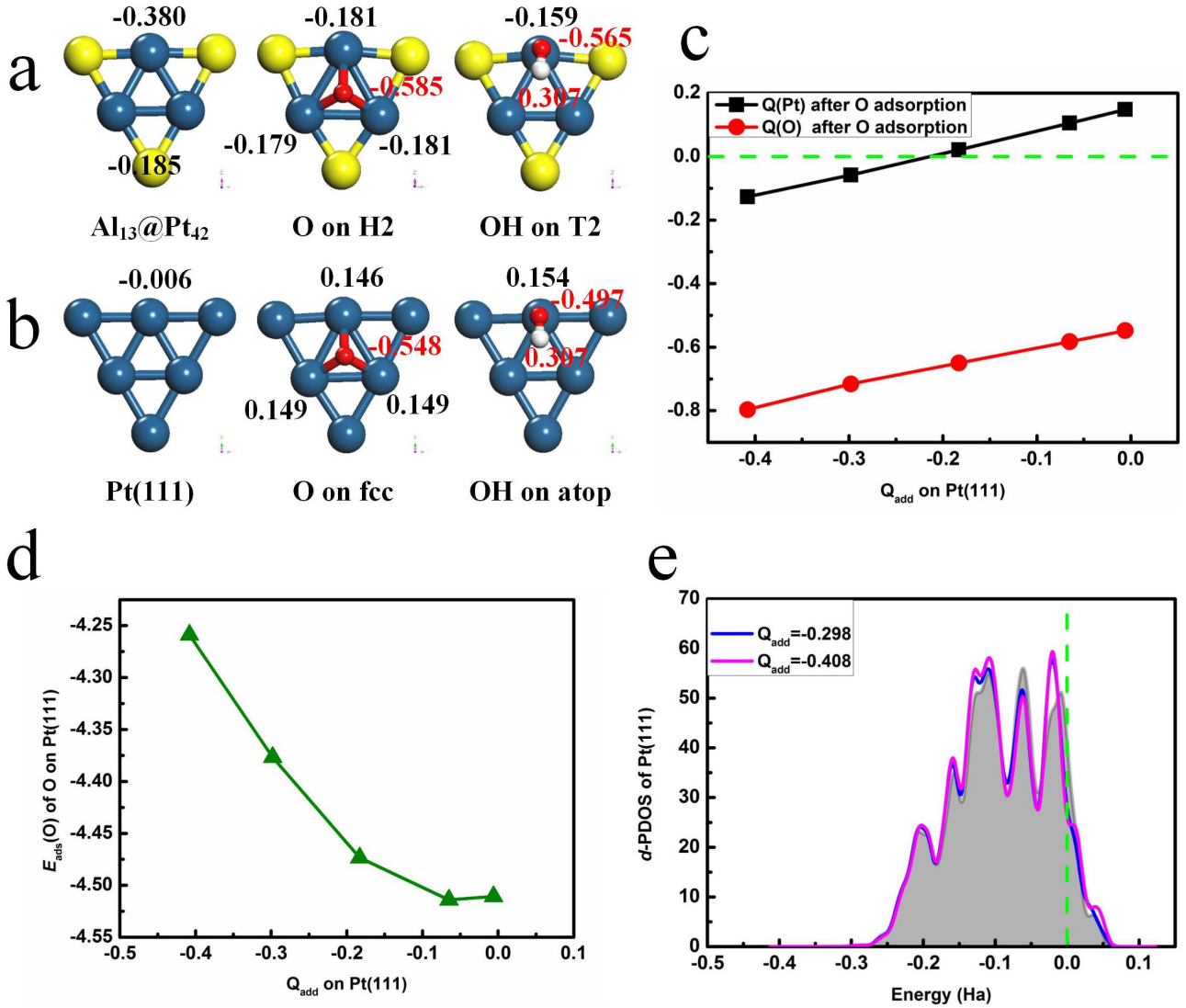

Figure 3 | The Mulliken charges Q of $Al_{13}@Pt_{42}$ (a) and Pt (111) (b). (c) The Mulliken charges Q on Pt(111) with different Q_{add}. (d) The E_{ads}(O) on Pt(111) with different Q_{add}. (e) The plot of *d*-electron PDOS of Pt(111) with different Q_{add}. For comparison, *d*-electron PDOS of Pt(111) without Q_{add} is shown in shaded. A negative value means electronic gain and a positive value means electronic loss.

projected onto the O-O bond where big change in PDOS is present. There is no spin polarization of the adsorbed O_2 orbitals, and the 5σ, 1π and 2π* orbitals of O_2 are broadened, which dominate the adsorption of O_2. It is clear that the partial antibonding orbital 2π* of adsorbed O_2 are filled compared with that in the gas phase. It is well known that partial population of the antibonding 2π* orbital of O_2 is responsible for the catalytic activation of the adsorbed O_2 and stretching of the O-O bond[48]. When O_2 is adsorbed on $Al_{13}@Pt_{42}$ with $E_{ads}(O_2) = -0.33$ eV, the corresponding O-O bond is 1.398 Å (the O-O bond of the gas state is 1.225 Å), due to this charge transfer to the 2π* orbital of O_2 (0.306 *e*). As results, the O_2 on $Al_{13}@Pt_{42}$ is activated and then dissociated with such a small E_a value.

Table 3 | The preferred activation energies (E_a) and reaction energies (E_r) for elemental steps in ORR. All results are in unit of eV

	$Al_{13}@Pt_{42}$		Pt(111)	
Reaction steps	E_a	E_r	E_a	E_r
$O_2 \rightarrow 2O$	0.13	−1.66	0.00	−2.18
$O + H \rightarrow OH$	0.59	−0.59	0.97	−0.07
$OH + H \rightarrow H_2O$	0.31	−1.11	0.24	−0.56
$H_2O \rightarrow H_2O$(gas)		0.41		0.58
$O_2 + H \rightarrow OOH$	0.81	−0.37	0.22	−0.19
$OOH \rightarrow O + OH$	0.28	−0.91	0.00	−2.07
$O + H_2O \rightarrow 2OH$	0.57	0.57	0.50	0.49
O(H1) → O(H2)	0.44		0.62–0.66	

[a]The O diffusion energy barrier on Pt(111) are from references [15,16], the H_2O desorption barrier is from reference [50]while other data on Pt(111) come from reference [18]

In light of Table 3, $E_a = 0.59$ eV for OH formation from O and H, which is forbidden on Pt(111) because of the high E_a of 0.97 eV[18]. It has been demonstrated that the large component of this E_a comes from O diffusion from hollow site to a bridge site, which is consistent with our results[15]. On $Al_{13}@Pt_{42}$, O is easier to diffuse with 0.44 eV diffusion barrier due to the lower E_{ads}(O) value compared with that of 0.62 or 0.66 eV on Pt(111)[15,16]. That is the reason why E_a value of $Al_{13}@Pt_{42}$ is smaller than that of Pt(111) for OH formation from O and H. Thus, the path for OH formation becomes feasible on $Al_{13}@Pt_{42}$. For H_2O formation, $E_a = 0.31$ eV, which is comparable with Pt(111)[18]. Similar with Pt(111), the disappearance of the OH diffusion makes E_a for H_2O formation lower than that for OH formation[16]. The last step is removal of the adsorbed H_2O and recovery the surface active site. Once H_2O is formed, it needs to overcome 0.41 eV for desorption.

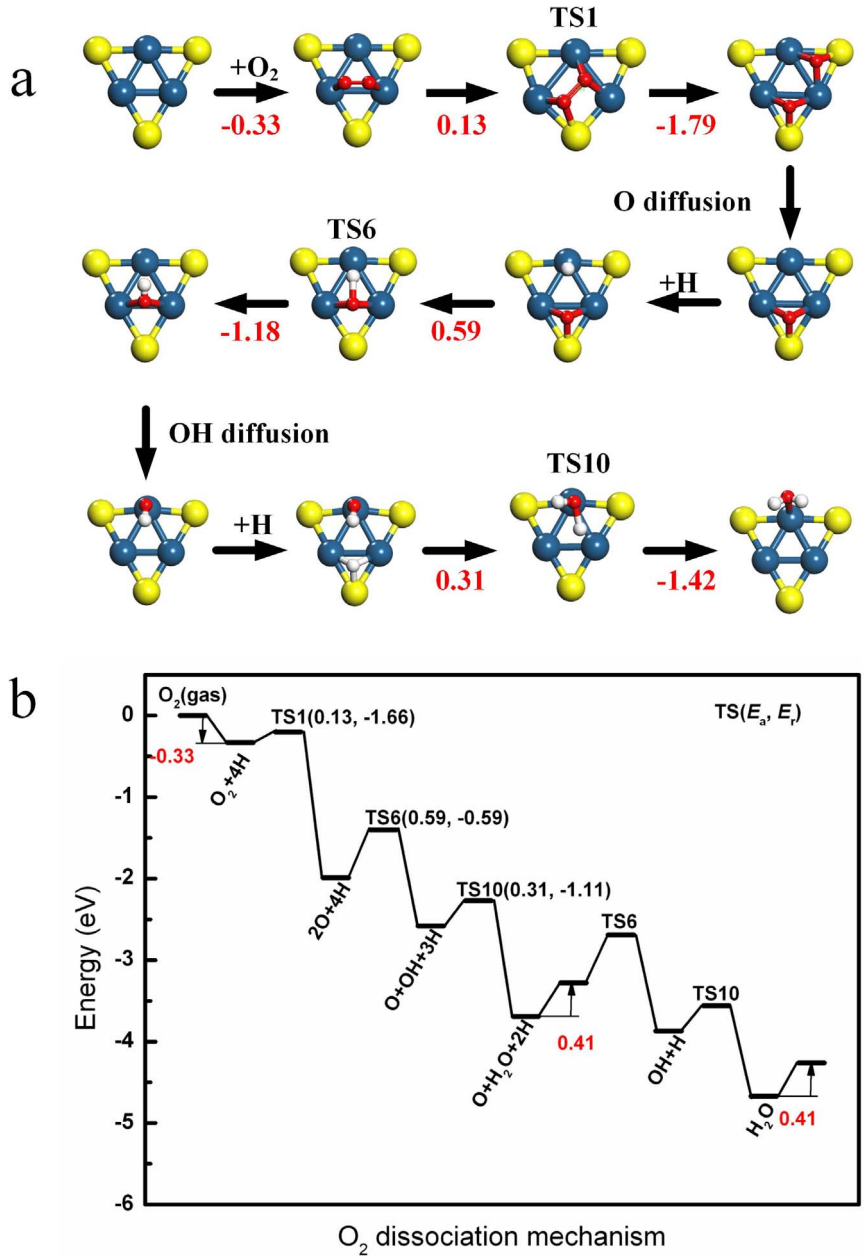

Figure 4 | Optimized overall reaction path of O_2 dissociation mechanism. (a) The structures of initial, transition and final states, respectively. (b) Schematic energy profile.

Discussion

Therein, as shown in Figure 4, the rate-limiting step (RDS) of O_2 dissociation mechanism is located at OH formation from O and H with E_a = 0.59 eV. On the other hand, for OOH associative mechanism, RDS is located at OOH formation with E_a = 0.81 eV and E_r = −0.37 eV. Since E_a value of RDS of O_2 dissociation mechanism is lower than that of OOH associative mechanism, the former is more effective. In addition, we have excluded the two-electron reduction to H_2O_2 since H_2O_2 spontaneous dissociates into OH on Al_{13}@Pt_{42}, which is consistent with experimental results on Pt and other Pt alloys[49]. When we observe the corresponding data of Pt(111) in Table 3, RDS is located at OH formation from O and H_2O with E_a = 0.50 eV[18,50]. E_a value for OH formation on Al_{13}@Pt_{42} is comparable with that on Pt(111). It is well known that when E_a < 0.75 eV, there is room temperature activity[51]. As results, Al_{13}@Pt_{42} can effectively catalyze ORR at room temperature.

In summary, the core-shell Al_{13}@Pt_{42} cluster is a good ORR candidate for the fuel cell application and possesses at least four superiorities listed below: (1) Excellent cluster stability due to the formation of the Al-Pt covalent bonds; (2) A better activity than Pt(111) due to the optimal O adsorption energy; (3) The maximal Pt atomic utilization of 70% due to the utility of the anti-poisoning edge Pt atoms with consideration of OH adsorption; (4) OH formation with E_a = 0.59 eV (being comparable with Pt(111) of 0.50 eV) as the RDS with O_2 dissociation mechanism.

Methods

Most calculations are performed within the DFT framework as implemented in DMol^3 code[52,53]. The generalized gradient approximation (GGA) with the Perdew–Burke–Ernzerhof (PBE) functional is employed to describe exchange and correlation effects[54]. The All Electron Relativistic (AER) core treat method is implemented for relativistic effects, which explicitly includes all electrons and introduces some relativistic effects into the core[55]. In this work, the double numerical atomic orbital augmented by a polarization *p*-function (DNP) is chosen as the basis set[52]. The orbital cutoff values are 4.5 Å and 4.8 Å for Pt_{55}/Pt(111) and Al_{13}@Pt_{42}, respectively, which lead to the difference of the atomic energies is within 0.1 eV atom^{-1}, compared with the cutoff value of 6.5 Å. Thus, the value satisfies the accuracy required. A smearing of 0.005 Ha (1 Ha = 27.21 eV) to the orbital occupation is applied to achieve accurate

electronic convergence. The spin-unrestricted method is used for all calculations. The convergence tolerance of energy is 1.0×10^{-5} Ha, maximum force is 0.002 Ha/Å, and maximum displacement is 0.005 Å in Dmol^3. Note that the DNP basis set is the most accurate for our studied systems in Dmol^3 code when Pt element is included in any considered system and is comparable to the Gaussian 6–31(d) basis[56] while DNP results have shown excellent consistency with experiments in literatures[57].

It is known that the cell size effect for the calculations of 38 atomic clusters is negligible when the size is large than 25 Å[58]. In our case, we consider the calculations of 55 atomic clusters. Thus, we have tested cubic boxes with sizes of 25 Å and 30 Å. The results are shown in Table S1. It is found from Table S1 that the results with sizes of 25 Å and 30 Å are consistent each other within energy difference smaller than 0.001 Ha. Thus, the box size of $25 \times 25 \times 25$ Å^3 is chosen for our system.

A three-layer $p(3 \times 3)$ periodic slab is taken to simulate Pt(111) surface where the two bottom layers are fixed. To confirm the reliability of this Pt(111) model, the E_{ads}(O) and E_{ads}(OH) values on a four-layer slab with two fixed layers and a five-layer slab with three fixed layers are calculated and listed in Table S2. It is shown that compared with the three-layer slab, the E_{ads}(O) and E_{ads}(OH) values on the two cases have errors of 0.03, which do not change all results what we have obtained. Therefore, our Pt(111) model has reasonable accuracy. The k-points are Gamma point for clusters and $(2 \times 2 \times 1)$ for Pt(111), respectively. The minimum energy paths (MEPs) for ORR are obtained by LST/QST tools in DMol^3 code.

A conductor-like screening model (COSMO) is used to simulate a H_2O solvent environment throughout the whole process in DMol^3 code[59] where the dielectric constant is set as 78.54 for H_2O solvent. It is noteworthy that this environment is necessary to describe the solvation[50]. To confirm this consideration, the adsorption energy values of O_2, O, H_2O and OH in gas and solvent environments are calculated and shown in Table S3. As shown in the table, there are evident differences in the both cases. For O_2, O and H_2O adsorption under solvent environment, E_{ads} are stronger while E_{ads}(OH) is weaker, compared with gas environment.

It is well known that there is the convergence failure of magnetic systems in DMol^3 code. To compare the stability among the different $M_{13}@Pt_{42}$ clusters, the core-shell interaction energy E_{cs} and the dissolution potentials of Pt_{42} shell $U_{diss}(M_{13}@Pt_{42})$ are calculated in CASTEP code with ultrasoft pseudopotentials[60]. The PBE is employed to describe exchange and correlation effects[54]. The use of a plane-wave kinetic energy cutoff of 400 eV is shown to give excellent convergence of total energies. The convergence tolerance of energy is 1.0×10^{-5} eV/atom, maximum force is 0.05 eV/Å, and maximum displacement is 0.005 Å in CASTEP. The 0.2 eV smearing is adopted for calculations.

To analyze the structural stability of alloy clusters with different numbers of Al atoms, the average binding energy of the cluster E_b is adopted,

$$E_b = (E_{cluster} - N_{Pt}E_{Pt} - N_{Al}E_{Al})/55 \quad (1)$$

where $E_{cluster}$, E_{Pt} and E_{Al} are the total energies of Pt_{55} or $Al_{13}@Pt_{42}$ clusters, Pt atom, and Al atom, respectively. N_{Pt} and N_{Al} denote the numbers of Pt and Al atoms.

The core-shell interaction energy E_{cs} is calculated as following,

$$E_{cs} = [E(M_{13}@Pt_{42}) - E(Pt_{42}) - E(M_{13})]/55 \quad (2)$$

where $E(M_{13}@Pt_{42})$, $E(Pt_{42})$ and $E(M_{13})$ are the total energies of $M_{13}@Pt_{42}$ clusters, Pt_{42} shell and M_{13} core, respectively.

Following the idea of Noh et al.[26], we define the dissolution potential of $M_{13}@Pt_{42}$ cluster as the lowest potential at which the Pt-skin layer dissolves into acidic solution. Specifically, we considered the electrochemical reaction of $M_{13}@Pt_{42}$ cluster of eq. (3),

$$M_{13}@Pt_{42} \rightarrow M_{13} + n_{shell}Pt^{2+} + 2n_{shell}e^- \quad (3)$$

where n_{shell} is the number of Pt atoms in the $M_{13}@Pt_{42}$ ($n_{shell} = 42$). The dissolution potential of the Pt_{42} shell is calculated by,

$$\begin{aligned} U_{diss}(M_{13}@Pt_{42}) &= U_{diss}(Pt_{bulk}) \\ &+ [E(M_{13}) + n_{shell}E(Pt_{bulk}) - E(M_{13}@Pt_{42})]/(2\ n_{shell}e) \end{aligned} \quad (4)$$

where $U_{diss}(M_{13}@Pt_{42})$ and $U_{diss}(Pt_{bulk})$ are the dissolution potentials of the outmost shell of $M_{13}@Pt_{42}$ clusters and that of a bulk Pt, respectively. $E(Pt_{bulk})$ denotes the total energy of bulk Pt. Here, $U_{diss}(Pt_{bulk}) = 1.188$ V.

The adsorption energies (E_{ads}) of adsorbates on these clusters are calculated through,

$$E_{ads} = E_{sys} - E_{species} - E_{catalyst} \quad (5)$$

where $E_{species}$, $E_{catalyst}$ and E_{sys} are the total energy of an isolated adsorbate species, the catalyst [Pt(111), Pt_{55} and $Al_{13}@Pt_{42}$] and the adsorption system, respectively. $E_{ads} < 0$ corresponds to an exothermic adsorption process.

1. Vinayan, B. P., Nagar, R., Rajalakshmi, N. & Ramaprabhu, S. Novel platinum–cobalt alloy nanoparticles dispersed on nitrogen-doped graphene as a cathode electrocatalyst for PEMFC applications. *Adv. Funct. Mater.* **22**, 3519–3526 (2012).
2. Nørskov, J. K. *et al.* Origin of the overpotential for oxygen reduction at a fuel-cell cathode. *J. Phys. Chem. B* **108**, 17886–17892 (2004).
3. Tritsaris, G., Greeley, J., Rossmeisl, J. & Nørskov, J. Atomic-scale modeling of particle size effects for the oxygen reduction reaction on Pt. *Catal. Lett.* **141**, 909–913 (2011).
4. Shao, M., Peles, A. & Shoemaker, K. Electrocatalysis on platinum nanoparticles: particle size effect on oxygen reduction reaction activity. *Nano Lett.* **11**, 3714–3719 (2011).
5. Sánchez-Sánchez, C. M. *et al.* Imaging structure sensitive catalysis on different shape-controlled platinum nanoparticles. *J. Am. Chem. Soc.* **132**, 5622–5624 (2010).
6. Viswanathan, V., Hansen, H. A., Rossmeisl, J. & Nørskov, J. K. Universality in oxygen reduction electrocatalysis on metal surfaces. *ACS Catal.* **2**, 1654–1660 (2012).
7. Yamamoto, K. *et al.* Size-specific catalytic activity of platinum clusters enhances oxygen reduction reactions. *Nat. Chem.* **1**, 397–402 (2009).
8. Lim, D. H. & Wilcox, J. Mechanisms of the oxygen reduction reaction on defective graphene-supported Pt nanoparticles from first-principles. *J. Phys. Chem. C* **116**, 3653–3660 (2012).
9. Stamenkovic, V. *et al.* Changing the activity of electrocatalysts for oxygen reduction by tuning the surface electronic structure. *Angew. Chem.* **118**, 2963–2967 (2006).
10. Lim, D. H. & Wilcox, J. DFT-based study on oxygen adsorption on defective graphene-supported Pt nanoparticles. *J. Phys. Chem. C* **115**, 22742–22747 (2011).
11. Karlberg, G. S., Rossmeisl, J. & Norskov, J. K. Estimations of electric field effects on the oxygen reduction reaction based on the density functional theory. *Phys. Chem. Chem. Phys.* **9**, 5158–5161 (2007).
12. Abild-Pedersen, F. *et al.* Scaling properties of adsorption energies for hydrogen-containing molecules on transition-metal surfaces. *Phys. Rev. Lett.* **99**, 016105 (2007).
13. Greeley, J. *et al.* Alloys of platinum and early transition metals as oxygen reduction electrocatalysts. *Nat. Chem.* **1**, 552–556 (2009).
14. Stephens, I. E. L. *et al.* Tuning the activity of Pt(111) for oxygen electroreduction by subsurface alloying. *J. Am. Chem. Soc.* **133**, 5485–5491 (2011).
15. Michaelides, A. & Hu, P. Catalytic water formation on platinum:afirst-principles study. *J. Am. Chem. Soc.* **123**, 4235–4242 (2001).
16. Qi, L., Yu, J. & Li, J. Coverage dependence and hydroperoxyl-mediated pathway of catalytic water formation on Pt (111) surface. *J. Chem. Phys.* **125**, 054701 (2006).
17. Keith, J. A., Jerkiewicz, G. & Jacob, T. Theoretical investigations of the oxygen reduction reaction on Pt(111). *ChemPhysChem* **11**, 2779–2794 (2010).
18. Sha, Y., Yu, T. H., Merinov, B. V., Shirvanian, P. & Goddard, W. A. Oxygen hydration mechanism for the oxygen reduction reaction at Pt and Pd fuel cell catalysts. *J. Phys. Chem. Lett.* **2**, 572–576 (2011).
19. Zhang, J., Vukmirovic, M. B., Xu, Y., Mavrikakis, M. & Adzic, R. R. Controlling the catalytic activity of platinum-monolayer electrocatalysts for oxygen reduction with different substrates. *Angew. Chem. Int. Edit.* **44**, 2132–2135 (2005).
20. Wu, J. *et al.* Icosahedral platinum alloy nanocrystals with enhanced electrocatalytic activities. *J. Am. Chem. Soc.* **134**, 11880–11883 (2012).
21. Stamenkovic, V. R. *et al.* Trends in electrocatalysis on extended and nanoscale Pt-bimetallic alloy surfaces. *Nat. Mater.* **6**, 241–247 (2007).
22. Stephens, I. E. L., Bondarenko, A. S., Gronbjerg, U., Rossmeisl, J. & Chorkendorff, I. Understanding the electrocatalysis of oxygen reduction on platinum and its alloys. *Energ. Environ. Sci.* **5**, 6744–6762 (2012).
23. Stamenkovic, V. R., Mun, B. S., Mayrhofer, K. J. J., Ross, P. N. & Markovic, N. M. Effect of surface composition on electronic structure, stability, and electrocatalytic properties of Pt-transition metal alloys: Pt-skin versus Pt-skeleton surfaces. *J. Am. Chem. Soc.* **128**, 8813–8819 (2006).
24. Jóhannesson, G. H. *et al.* Combined electronic structure and evolutionary search approach to materials design. *Phys. Rev. Lett.* **88**, 255506 (2002).
25. Piotrowski, M. J., Piquini, P. & Da Silva, J. L. F. Platinum-based nanoalloys Pt_nTM_{55-n} (TM = Co, Rh, Au): a density functional theory investigation. *J. Phys. Chem. C* **116**, 18432–18439 (2012).
26. Noh, S., Seo, M., Seo, J., Fischer, P. & Han, B. First principles computational study on the electrochemical stability of Pt-Co nanocatalysts. *Nanoscale* **5**, 8625–8633 (2013).
27. Wang, C. *et al.* Design and synthesis of bimetallic electrocatalyst with multilayered Pt-skin surfaces. *J. Am. Chem. Soc.* **133**, 14396–14403 (2011).
28. Colón-Mercado, H. R. & Popov, B. N. Stability of platinum based alloy cathode catalysts in PEM fuel cells. *J. Power Sources* **155**, 253–263 (2006).
29. Greeley, J. & Nørskov, J. K. Combinatorial density functional theory-based screening of surface alloys for the oxygen reduction reaction. *J. Phys. Chem. C* **113**, 4932–4939 (2009).
30. Chuang, F. C., Wang, C. Z. & Ho, K. H. Structure of neutral aluminum clusters $Al_n(2 \leq n \leq 23)$: genetic algorithm tight-binding calculations. *Phys. Rev. B* **73**, 125431 (2006).
31. Akola, J., Häkkinen, H. & Manninen, M. Ionization potential of aluminum clusters. *Phys. Rev. B* **58**, 3601–3604 (1998).
32. Ecker, A., Weckert, E. & Schnockel, H. Synthesis and structural characterization of an Al_{77} cluster. *Nature* **387**, 379–381 (1997).
33. Mandal, S., Wang, J., Winans, R. E., Jensen, L. & Sen, A. Quantum size effects in the optical properties of ligand stabilized aluminum nanoclusters. *J. Phys. Chem. C* **117**, 6741–6746 (2013).
34. Wang, Y. *et al.* Thermite reactions of Al/Cu core-shell nanocomposites with WO_3. *Thermochimica Acta* **463**, 69–76 (2007).

35. Cheng, Z., Li, F., Yang, Y., Wang, Y. & Chen, W. A facile and novel synthetic route to core–shell Al/Co nanocomposites. *Mater. Lett.* **62**, 2003–2005 (2008).
36. Chen, Y., Yang, F., Dai, Y., Wang, W. & Chen, S. Ni@Pt core–shell nanoparticles: synthesis, structural and electrochemical properties. *J. Phys. Chem. C* **112**, 1645–1649 (2008).
37. Kristian, N., Yu, Y., Lee, J. M., Liu, X. & Wang, X. Synthesis and characterization of Co_{core}–Pt_{shell} electrocatalyst prepared by spontaneous replacement reaction for oxygen reduction reaction. *Electrochem. Acta* **56**, 1000–1007 (2010).
38. Jang, J. H. *et al.* Rational syntheses of core-shell Fex@Pt nanoparticles for the study of electrocatalytic oxygen reduction reaction. *Sci. Rep.* **3**, 2872 (2013).
39. Greeley, J. & Nørskov, J. K. Electrochemical dissolution of surface alloys in acids: thermodynamic trends from first-principles calculations. *Electrochem. Acta* **52**, 5829–5836 (2007).
40. Kattel, S., Duan, Z. & Wang, G. Density dunctional theory study of an oxygen reduction reaction on a Pt_3Ti alloy electrocatalyst. *J. Phys. Chem. C* **117**, 7107–7113 (2013).
41. Lin, X. *et al.* Effect of particle size on the adsorption of O and S atoms on Pt: A density-functional theory study. *J. Phys. Chem. B* **105**, 7739–7747 (2001).
42. Koper, M. T. M., Shubina, T. E. & van Santen, R. A. Periodic density functional study of CO and OH adsorption on Pt–Ru alloy surfaces: implications for CO tolerant fuel cell catalysts. *J. Phys. Chem. B* **106**, 686–692 (2001).
43. Hammer, B. & Nørskov, J. K. Theoretical surface science and catalysis-calcutions and concepts. *Adv. Catal.* **45**, 71–129 (2000).
44. Friebel, D. *et al.* Balance of nanostructure and bimetallic interactions in Pt model fuel cell catalysts: in situ XAS and DFT study. *J. Am. Chem. Soc.* **134**, 9664–9671 (2012).
45. Koper, M. T. M. & van Santen, R. A. Interaction of H, O and OH with metal surfaces. *J. Electroanal. Chem.* **472**, 126–136 (1999).
46. Feibelman, P. J. *d*-electron frustration and the large fcc versus hcp binding preference in O adsorption on Pt(111). *Phys. Rev. B* **56**, 10532–10537 (1997).
47. Zhang, P., Zheng, W. T. & Jiang, Q. Behaviors of monomer H_2O on the Cu(111) surface under surface sharges. *J. Phys. Chem. C* **114**, 19331–19337 (2010).
48. Coquet, R., Howard, K. L. & Willock, D. J. Theory and simulation in heterogeneous gold catalysis. *Chem. Soc. Rev.* **37**, 2046–2076 (2008).
49. Stamenkovic, V. R. *et al.* Improved oxygen reduction qctivity on $Pt_3Ni(111)$ via increased surface site svailability. *Science* **315**, 493–497 (2007).
50. Sha, Y., Yu, T. H., Liu, Y., Merinov, B. V. & Goddard, W. A. Theoretical study of solvent effects on the platinum-catalyzed oxygen reduction reaction. *J. Phys. Chem. Lett* **1**, 856–861 (2010).
51. Shang, C. & Liu, Z. P. Origin and activity of gold nanoparticles as aerobic oxidation catalysts in aqueous solution. *J. Am. Chem. Soc.* **133**, 9938–9947 (2011).
52. Delley, B. An all-electron numerical method for solving the local density functional for polyatomic molecules. *J. Chem. Phys.* **92**, 508–517 (1990).
53. Delley, B. From molecules to solids with the $DMol^3$ approach. *J. Chem. Phys.* **113**, 7756–7764 (2000).
54. Perdew, J. P., Burke, K. & Ernzerhof, M. Generalized gradient approximation made simple. *Phys. Rev. Lett.* **77**, 3865–3868 (1996).
55. Koelling, D. D. & Harmon, B. N. A technique for relativistic spin-polarised calculations. *J. Phys. C: SolidStatePhys.* **10**, 3107–3114 (1977).
56. Liu, P. & Rodriguez, J. A. Catalysts for hydrogen evolution from the [NiFe] hydrogenase to the $Ni_2P(001)$ surface: the impottance of ensemble effect. *J. Am. Chem. Soc.* **127**, 14871–14878 (2005).
57. Rodriguez, J. A. *et al.* Activity of CeO_x and TiO_x nanoparticles grown on Au(111) in the water-gas shift reaction. *Science* **318**, 1757–1760 (2007).
58. Lin, R. J., Chen, H. L., Ju, S. P., Li, F. Y. & Chen, H. T. Quantum-chemical calculations on the mechanism of the water–gas shift reaction on nanosized gold cluster. *J. Phys. Chem. C* **116**, 336–342 (2011).
59. Todorova, T. & Delley, B. Wetting of paracetamol surfaces studied by $DMol^3$-COSMO calculations. *Mol. Simul.* **34**, 1013–1017 (2008).
60. Vanderbilt, D. Soft self-consistent pseudopotentials in a generalized eigenvalue formalism. *Phys. Rev. B* **41**, 7892–7895 (1990).

Acknowledgments

This work was supported by the National Key Basic Research Development Program (No. 2010CB631001), the National Natural Science Foundation of China (No. 51201069), the Key grant Project of Chinese Ministry of Education (No. 313026), the Program for New Century Excellent Talents in University (No. NCET-10-0437), and the Research Fund for the Doctoral Program of Higher Education of China (No. 20120061120042).

Author contributions

Y.F.Z. and Q.J. conceived and designed the material. B.B.X. carried out the simulation. B.B.X., Y.F.Z. and Q.J. wrote the paper. X.Y.L. and Z.W. entered the discussion. All authors commented on the manuscript.

Additional information

Supplementary information accompanies this paper at http://www.nature.com/scientificreports

Competing financial interests: The authors declare no competing financial interests.

How to cite this article: Xiao, B.B., Zhu, Y.F., Lang, X.Y., Wen, Z. & Jiang, Q. Al_{13}@Pt_{42} Core-Shell Cluster for Oxygen Reduction Reaction. *Sci. Rep.* **4**, 5205; DOI:10.1038/srep05205 (2014).